Three-dimensional reciprocal space x-ray coherent scattering tomography of two-dimensional object

Zheyuan Zhu and Shuo Pang[a)]
The College of Optics and Photonics, CREOL, University of Central Florida, Orlando, FL 32816, USA

(Received 4 June 2017; revised 1 December 2017; accepted for publication 5 February 2018; published 13 March 2018)

Purpose: X-ray coherent scattering tomography is a powerful tool in discriminating biological tissues and bio-compatible materials. Conventional x-ray scattering tomography framework can only resolve isotropic scattering profile under the assumption that the material is amorphous or in powder form, which is not true especially for biological samples with orientation-dependent structure. Previous tomography schemes based on x-ray coherent scattering failed to preserve the scattering pattern from samples with preferred orientations, or required elaborated data acquisition scheme, which could limit its application in practical settings. Here, we demonstrate a simple imaging modality to preserve the anisotropic scattering signal in three-dimensional reciprocal (momentum transfer) space of a two-dimensional sample layer.

Methods: By incorporating detector movement along the direction of x-ray beam, combined with a tomographic data acquisition scheme, we match the five dimensions of the measurements with the five dimensions (three in momentum transfer domain, and two in spatial domain) of the object. We employed a collimated pencil beam of a table-top copper-anode x-ray tube, along with a panel detector to investigate the feasibility of our method.

Results: We have demonstrated x-ray coherent scattering tomographic imaging at a spatial resolution ~2 mm and momentum transfer resolution 0.01 $Å^{-1}$ for the rotation-invariant scattering direction. For any arbitrary, non-rotation-invariant direction, the same spatial and momentum transfer resolution can be achieved based on the spatial information from the rotation-invariant direction. The reconstructed scattering profile of each pixel from the experiment is consistent with the x-ray diffraction profile of each material. The three-dimensional scattering pattern recovered from the measurement reveals the partially ordered molecular structure of Teflon wrap in our sample.

Conclusions: We extend the applicability of conventional x-ray coherent scattering tomography to the reconstruction of two-dimensional samples with anisotropic scattering profile by introducing additional degree of freedom on the detector. The presented method has the potential to achieve low-cost, high-specificity material discrimination based on x-ray coherent scattering. [https://doi.org/10.1002/mp.12813]

Key words: coherent scattering, computed tomography (CT), small-angle x-ray scattering (SAXS)

1. INTRODUCTION

Biological soft tissues or bio-compatible materials, due to their low atomic weight and similar densities, do not exhibit strong contrast on conventional attenuation-based computed tomography (CT) image. By measuring the elastically scattered x-ray photons from the samples, small-angle x-ray scattering (SAXS) reveals richer information about their molecular composition and structure. X-ray scattering signature has been demonstrated as a high-contrast modality in distinguishing different types of tissues for medical imaging.[1–4] If the materials are amorphous or in the fine powder form, the SAXS profile is isotropic, and the tomographic reconstruction of a scalar SAXS profile from each pixel can be obtained from a projection setup similar to conventional CT. This method is termed coherent scattering computed tomography (CSCT), which has shown its success in resolving material-specific scattering profiles,[5–7] and has also been demonstrated feasible in medical imaging settings.[8,9] The requirement on isotropic scattering signal guarantees that the scattering from an object voxel remains unchanged regardless of the incident direction of x-ray, and thus, the projection data contributed from the same voxel is invariant under different projection angles. As a result, conventional CSCT can only reconstruct the coherent scattering profile in terms of the magnitude of momentum transfer, not the complete SAXS pattern, which is a function of the three-dimensional momentum transfer vector. However, the isotropic scattering assumption on the material is not true in some biological or bio-compatible samples. For example, tissues such as bones and teeth,[10,11] as well as bio-compatible polymers used in medical implants,[12] possess anisotropic scattering profile due to the existence of partially ordered structure at molecular level. Imaging the cellular formation within biomaterials is an indispensable step in evaluating the different

stages of tissue formation and regeneration.[13] While x-ray scattering is possible to obtain improved contrast among biological tissues, the anisotropic scattering profile could falsify the image reconstruction because it violates the rotation-invariant requirement in conventional CSCT. In addition, in security screening, many explosives comprise of crystalline structures. The preferred orientation of crystal grains could cause inconsistent intensity ratio among x-ray diffraction peaks, which is the main cause of false alarm.[14]

Several x-ray scattering tomography schemes have been developed to preserve the anisotropic scattering signal. The most straightforward strategy is to extend the concept of direct tomography,[15–17] which uses collimators in front of the detector to constrain the scattering direction, so that a snapshot of the spatial profile under a specific momentum transfer vector is obtained. The use of collimators decouples the scattering direction from the spatial profile of the sample, and therefore, the three-dimensional vector momentum transfer space of each voxel can be easily measured by positioning the collimators under different orientations. However, the collection efficiency is severely limited by the collimator, resulting in lengthy integration time for each snapshot image. Conventional SAXS tomography, which combines two-dimensional SAXS images with tomographic scan, reconstructs the spatial profile only along the rotation-invariant scattering direction,[18,19] leaving a large portion of the collected scattering image unused. Recent advancement in this technique added the tilt of rotational axis to the data acquisition scheme and demonstrated the reconstruction of full three-dimensional real and reciprocal space of the sample.[20] However, such systems require a synchrotron source and a complicated rotation motion, which limits its application in practical settings. Moreover, for imaging a two-dimensional slice within a three-dimensional object, or a thin slice of flat object, this data acquisition scheme suffers from dimension insufficiency, since tilting the rotational axis and raster scan perpendicular to the sample slice does not capture more information about the slice of interest.

In this paper, we extend the dimension of a pencil-beam scattering model with a series of 2D snapshots along the beam direction, which resolves the 2D scattering pattern from each point along the pencil beam. Combined with a tomographic data acquisition scheme consisting of sample translation and rotation, a total of five dimensions are acquired in the measurement, allowing us to reconstruct the three-dimensional scattering profile inside a two-dimensional sample slice through matching the dimensions between the object and measurement. Our method does not require collimators in front of the detector to decouple the scattering direction from the spatial profile. Therefore, we are able to achieve higher collection efficiency, which also allows us to use only a table-top source for SAXS measurement. In addition, by eliminating the sample tilt in SAXS tomography, our method is fully compatible with conventional CSCT setup and can be an add-on module when reconstructing anisotropic scattering profile.

2. METHODS AND MATERIALS

2.A. Direction-dependent x-ray coherent scattering

We start with resolving the scattering profile associated with a row of pixels integrated along a single x-ray beam. Figure 1 shows the geometry of a pencil-beam x-ray coherent scattering setup. The system employs a copper-anode x-ray tube (XRT60, Proto Manufacturing), which emits a sharp Kα line ($\Delta E \,/\, E_0 < 0.1$) centering around $E_0 = 8$ keV, as shown in Fig. 2. The incident x-ray spectrum can be approximated by a delta-function $S(E) = I_0\delta(E - E_0)$. The diverging x-ray source is collimated by a pair of pinholes to a narrow beam propagating along the z direction. The number of coherent scattering photons dI from a single object voxel toward the detector pixel located at $\mathbf{r}_d$ is given by the following:

$$dI = I_0 \int_E S(E)\frac{{r_e}^2}{2}(1+\cos^2\theta)\alpha(t)f(t,\mathbf{q})\beta(t,\theta)\mathrm{d}\Omega\mathrm{d}V\mathrm{d}\mathbf{q}\mathrm{d}E \tag{1}$$

where r_e is the classical electron radius, θ is the scattering angle, and the $\cos\theta \approx 1$ for small-angle scattering. The object function $f(t,\mathbf{q}) = n_0(t)|F(t,\mathbf{q})|^2$, which is the product between material density $n_0(t)$ and the square of molecular form factor $F(t,\mathbf{q})$; t, is the depth of object voxel along the beam; $\mathrm{d}V = A\mathrm{d}t$, which is the volume of the object voxel illuminated by the x-ray beam with cross-sectional area A; $\mathrm{d}\Omega = \Delta^2/|\mathbf{r}_d - t\hat{z}|^2$, which denotes the solid angle covered by a detector pixel with pixel size Δ located at $\mathbf{r}_d = (x_d, y_d, z_d)$. The delta-function spectrum integrates to a constant I_0. $\alpha(t)$ and $\beta(t,\theta)$ represent the attenuation on the incident and scattered beams, respectively. The momentum transfer vector $\mathbf{q} = \mathbf{k}' - \mathbf{k}_0$, defined as the change in the wave vector between incident and scattered x-ray, is given by the vector form of Bragg's law:

$$\mathbf{q} = \frac{E}{hc}\left(\frac{\mathbf{r_d} - t\hat{z}}{|\mathbf{r_d} - t\hat{z}|} - \hat{z}\right), \tag{2}$$

where E denotes the energy of the quasi-monochromatic x-ray source, h is Planck constant, and c is the speed of light.

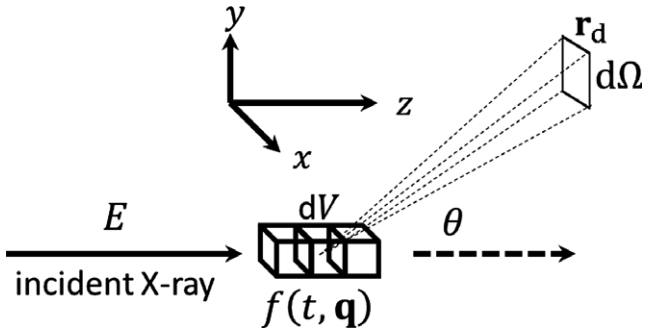

FIG. 1. Pencil-beam coherent scattering model applied to vector momentum transfer. Each pixel on a panel detector receives the scattering from all the pixels illuminated by the pencil beam under different momentum transfer vectors.

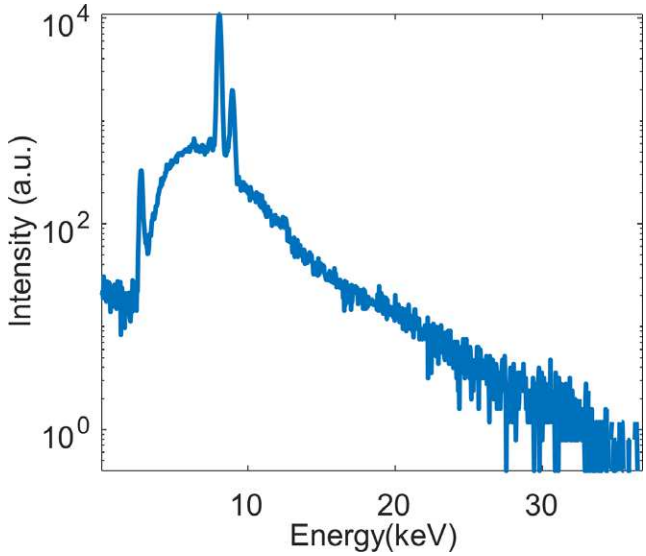

FIG. 2. Power spectrum of copper-anode x-ray source in log scale. [Color figure can be viewed at wileyonlinelibrary.com]

According to Eq. (2), the detector plane at a fixed location, z_d, covers a curved Ewald sphere in three-dimensional $\mathbf{q}$ space. If the distance between the object voxel and detector, $(z_d - t)$, is much greater than the horizontal (vertical) offset of the detector pixel, $x_d(y_d)$, we can ignore them on the denominator. The vector form of Bragg's law can be simplified to

$$\mathbf{q} = \frac{E}{hc}\left(\frac{x_d\hat{x} + y_d\hat{y}}{z_\mathbf{d} - t}\right), \tag{3}$$

which indicates that under small-angle approximation, the Ewald sphere becomes a flat section defined by the plane $q_z = 0$ in the momentum transfer space. The detector plane can be expressed in terms of the cylindrical coordinates by defining $w = (x_d^2 + y_d^2)^{1/2}$ and $\psi = \arctan(y_d/x_d)$ as the distance and azimuthal angle of each detector pixel with respect to the center of detector. Rewriting Eq. (3) in cylindrical coordinates and combining with Eq. (1), the intensity detected by the detector pixel located at $\mathbf{r}_d$ can be expressed in the cylindrical coordinate as follows:

$$g(w, z_d, \psi) = \int\int r_e{}^2 f(t, \mathbf{q})\delta\left[\mathbf{q} - \frac{E}{hc}\left(\frac{w\hat{r}}{z_d - t}\right)\right]\frac{\Delta^2}{w^2 + (z_d - t)^2}A\mathrm{d}t\mathrm{d}\mathbf{q}, \tag{4}$$

where $\hat{r} = (\cos\psi, \sin\psi, 0)$ is the unit vector along the radial direction. Due to the confinement of the scattering volume in the x-y plane under pencil-beam illumination, the $\mathbf{q}$ vector probed by Bragg's law contains only the radial component $\mathbf{q} = Ew/(hc(z_d - t))\hat{r}$. Therefore, the radial and azimuthal directions in the momentum transfer space can be separated by expressing the $\mathbf{q}$ vector on the section of $q_z = 0$ plane as $\mathbf{q} = q_r\hat{r}$, where $q_r = (q_x^2 + q_y^2)^{1/2}$ is the magnitude of the $\mathbf{q}$ vector on $q_z = 0$ plane and $\hat{r}$ is the unit vector along radial direction under azimuthal angle $\psi = \arctan(q_y/q_x)$. As a result, the integral on the $\mathbf{q} - t$ hyperplane in Eq. (4) is confined to the 2D $q_r - t$ plane under each azimuthal angle ψ. By moving the detector and capturing different scattering images along z direction, the resulting measurement establishes a linear mapping between the object domain $(t, q_r)_\psi$ and the measurement domain $(w, z_d)_\psi$. By discretizing the object with sampling rate Δt in spatial domain and Δq in momentum transfer domain, and partitioning the panel detector into square pixels with pitch Δ and step size Δz_d along the beam direction, Eq. (4) can be written in the form of a linear system $\mathbf{g} = \mathbf{Hf}$, where the system matrix is constructed based on the weight of each object voxel calculated from the term $\Delta^2/(w^2 + (z_d - t)^2)\mathrm{d}t\mathrm{d}\mathbf{q}$. A special case of this model using the scattering images from two detector locations z_d has been demonstrated.[21]

2.B. Measurement scheme

The three degrees of freedom in the pencil-beam measurement, two from the panel detector and one from the detector movement, enable the recovery of three-dimensional scattering volume along each pixel hit by x-ray. To resolve the three-dimensional $\mathbf{q}$-space within a two-dimensional sample slice, a tomographic data acquisition scheme, combining the sample rotation ϕ around y direction and translation s along x direction, is introduced to the pencil-beam system model, as shown in Fig. 3(a). To facilitate the discussion of the tomography geometry, we establish an object coordinate that translates and rotates with the sample, and express a total of five dimensions associated with the spatial and momentum transfer domain of the sample in terms of the object coordinate $f_o(\mathbf{r}_o, \mathbf{q}_o)$. Without any rotation or sample translation, the x, y, and z directions of the sample coordinate co-align with those of the laboratory coordinate. The slice imaged by our system is defined as $y_o = 0$. Under specific projection angle, ϕ, and sample translation, s, the object function probed by the pencil-beam coherent scattering system becomes a series of 2D sections in momentum transfer space along a row of voxels illuminated by the beam:

$$f_{s,\phi}(t, \mathbf{q}) = f_o(\mathbf{A}_\phi(s, 0, t)^T, \mathbf{A}_\phi\mathbf{q}), \tag{5}$$

where $\mathbf{A}_\phi$ is the 3 by 3 rotation matrix around y axis with rotation angle ϕ. Combining the pencil-beam model in Eq. (4) with the tomographic geometry in Eq. (5), a total of five dimensions are collected in our measurement scheme for the reconstruction of $f_o(x, y = 0, z, q_x, q_y, q_z)$:

$$g_{s,\phi}(w, z_d, \psi) = \int\int r_e{}^2 f_o(\mathbf{A}_\phi(s, 0, t)^T, \mathbf{A}_\phi\mathbf{q})\delta\left[\mathbf{q} - \frac{E}{hc}\left(\frac{w\hat{r}}{z_d - t}\right)\right]\frac{\Delta^2}{w^2 + (z_d - t)^2}A\mathrm{d}t\mathrm{d}\mathbf{q}. \tag{6}$$

Our x-ray tube (XRT60, Proto Manufacturing) is a copper-anode source operating under 45 kV and 40 mA without any filtration. The spectrum of the source is measured with a

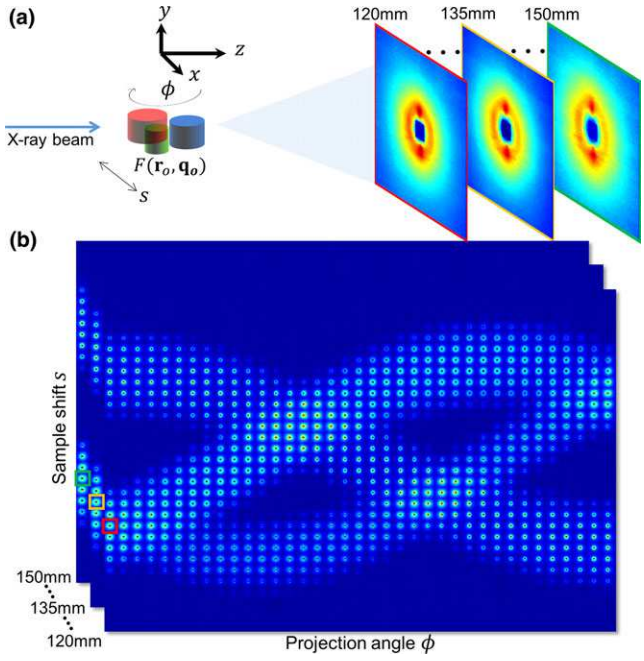

FIG. 3. (a) Measurement scheme of the three-dimensional momentum transfer space inside an extended object, which consists of sample translation and rotation in addition to the pencil-beam coherent scattering model. (b) The five-dimensional measurement consists of a series of 4D sinograms along the z direction. Each pixel in the sinogram under a specific z_d consists of an entire 2D scattering image. The three squares on the sinogram correspond to the scattering images enclosed in red, yellow, and green in (a). [Color figure can be viewed at wileyonlinelibrary.com]

photon-counting detector (X-123, AMPTEK). To implement the system geometry illustrated in Fig. 3(a), a pair of 2-mm pinholes were placed downstream the source to collimate the x-ray into a pencil beam. The sample was mounted on a rotational stage (RV1200P, Newport) and a translation stage (UTM150CC, Newport) as in a pencil-beam CT setup. The step size of the translation stage was set to 1 mm to match the Nyquist sampling rate given the 2 mm width of our x-ray beam. The sample is rotated from 0° to 180° at a step of 5°. The scattered x-rays emerging from the sample was captured by a flat panel detector (1215CF-MP, Rayence), which was also mounted on a translation stage (UTM150CC, Newport) to scan a series of 2D snapshots under different distances to the sample. The effective pixel size on the detector is 200 × 200 μm after binning. The exposure time for each scattering image was 30 s, resulting in a total acquisition time of 10 h for the conventional CSCT scan. The distance between the detector and the sample was changed from 120 to 150 mm at a step size of 3 mm to capture a series of 2D images along z direction. The detector scan along z direction was performed from 0° to 180° projections at a step of 30° to capture 7 sections in the 3D momentum transfer space. Each detector scan along z direction took 8 min. The total imaging time depends on the number of 2D sections captured in the 3D momentum transfer space, and in our case, it was around 11 h. The position of the detector was carefully aligned in a way that the pencil beam would always hit its center as it moves along z direction. The central 10 × 10 mm region on the detector was covered by a beam stop made of 1/8inch-thick lead sheet. The sample consisted of three isolated cylindrical tubes containing butter, Teflon wrap and water, each being approximately 8 mm in diameter and separated around 10 mm apart from each other. There was a small tilt of the Teflon wrap in the x-y plane with respect to the rotation axis. The five-dimensional measurement as a result of sample shift, rotation, and detector translation is shown in Fig. 3(b), which is a series of four-dimensional sinograms along z_d. Each pixel on the 4D sinogram contains an entire 2D scattering image $g_{s,\phi}(x_d, y_d)$ rather than a single value as the attenuation-based CT.

3. RECONSTRUCTION AND RESULTS

For a fixed detector location, z_d, and $\psi = 90°$ on the detector plane, the unit vector $\hat{r}$ in Eq. (4) becomes $\hat{y}$, and therefore, only the momentum transfer vector $\mathbf{q} = q_y\hat{y}$ is captured by the pencil-beam system. Since the vector $\hat{y}$ is invariant to matrix $\mathbf{A}_\phi$ under all projection angles, the same momentum transfer q_y is probed for all the object voxels as the sample rotates, which matches the assumption of conventional CSCT. Eq. (6) can be simplified for $\psi = 90°$ as

$$g_{s,\phi}(w) = {r_e}^2 \frac{\Delta^2}{w^2 + (z_d - t)^2} A \int f_o(s\cos\phi + t\sin\phi, 0, -s\sin\phi + t\cos\phi, \frac{E}{hc}\left(\frac{w}{z_d - t}\right)\hat{y})\mathrm{d}t. \quad (7)$$

The projection transform in Eq. (7) can be treated as a line integral on the $q_y - t$ plane along a family of curves $q_y = Ew/(hc(z_d - t))$ with w as a parameter. The tomographic reconstruction on a subset of the object function $f_o(x, 0, z, 0, q_y, 0)$ is implemented using the angular-dispersive coherent scattering computed tomography (AD-CSCT) scheme,[22] which establishes a backprojection from the measurement domain (s, ϕ, w) to the object domain (x, z, q_y). The sampling is 1 mm in the spatial domain, and 0.005 $\mathring{\mathrm{A}}^{-1}$ along q_y direction. The AD-CSCT reconstruction from a subset of measurement data $g_{s,\phi}(w; z_d = 120mm, \psi = 90°)$ is summarized in Fig. 4.

Figure 4(a) shows a normalized transmission map from a CT scan of the sample. The spatial profiles of the sample reconstructed from the intensity along the vertical radial direction on the detector are shown in Fig. 4(b1)–4(b3), corresponding to q_y = 0.08, 0.12 and 0.16 $\mathring{\mathrm{A}}^{-1}$, respectively. On a conventional CT image, water appears stronger than butter due to its high x-ray attenuation coefficient. However, the contrast between water and butter exhibits differently on CSCT images due to the higher scattering peak of water compared with butter. Therefore, at low momentum transfer, water appears to be a weaker scatter than butter, while the contrast between water and the butter reverses at high momentum transfer value. The reconstructed scattering

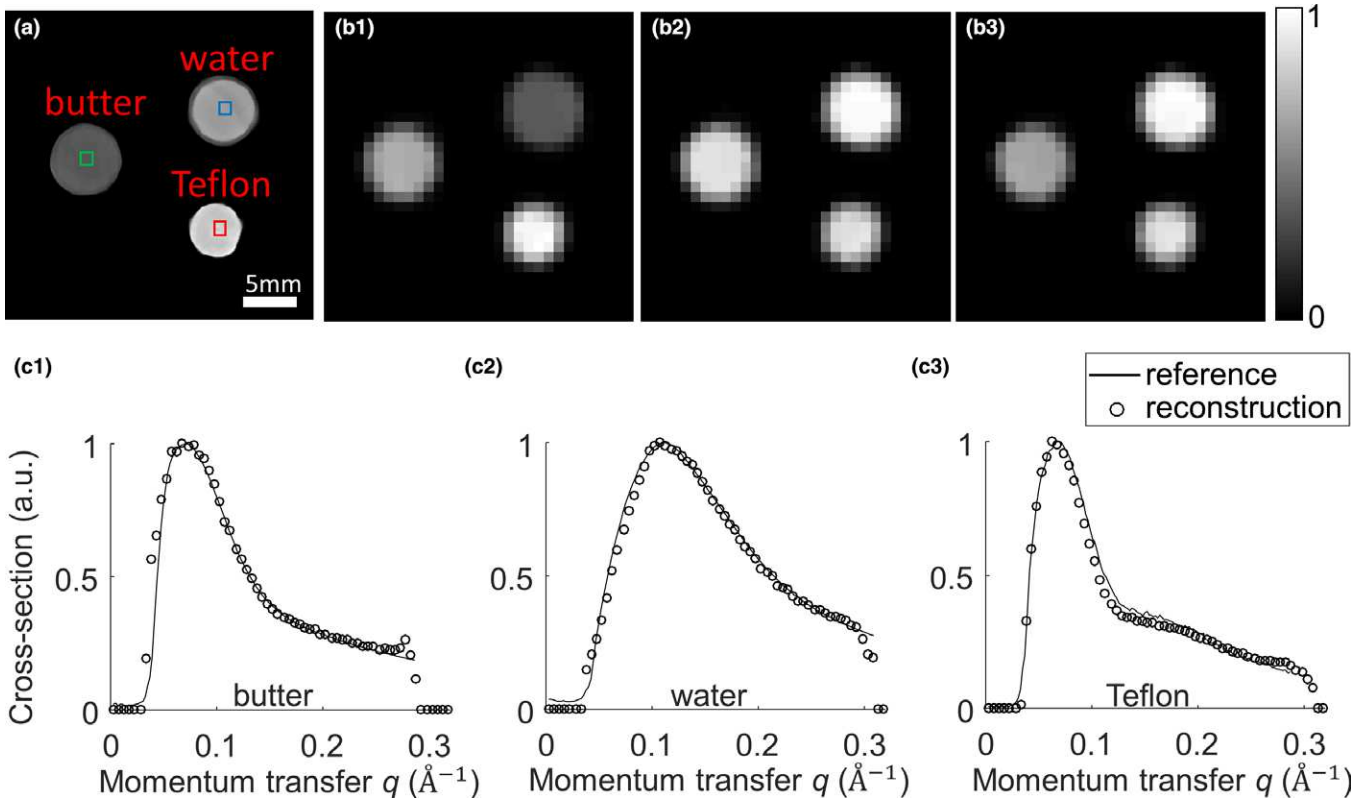

FIG. 4. (a) Transmission CT image of the phantom. (b1–b3) The spatial profile under momentum transfer values of 0.08, 0.12, and 0.16 Å^{-1} along the vertical direction. (c1–c3) The scattering profiles of the pixels in the region of butter, water and Teflon in (a). [Color figure can be viewed at wileyonlinelibrary.com]

profiles of three pixels marked in green, blue, and red, corresponding to butter, water and Teflon, are compared with their reference profiles in Fig. 4(c1)–4(c3), respectively. To collect the reference scattering profile, each material was shaped into a 2-mm-wide tip, illuminated by the same pencil beam used for tomography scan. Only the intensity along the vertical direction on the resultant 2D scattering image was picked as the reference. Figure 4(c) indicates a high consistency between the reconstructed scattering profile and that of the individual material, with error mainly in the high momentum transfer values, under which the scattering signal-to-noise ratio is low.

Both the setup geometry and the energy spectrum of the source contribute to the momentum transfer resolution of conventional CSCT. Differentiating the Bragg's law along the radial direction in Eq. (4) with respect to t, w, and E yields the uncertainty of the momentum transfer, Δq

$$\Delta q = \sqrt{\left(\frac{E}{hc}\frac{\Delta w}{z_d - t}\right)^2 + \left(\frac{E}{hc}\frac{w\Delta t}{(z_d - t)^2}\right)^2 + \left(\frac{\Delta E}{hc}\frac{w}{(z_d - t)}\right)^2}, \tag{8}$$

where $\Delta w = 0.4$ mm is the effective pixel size of the detector after binning; ΔE is the spectrum width at the Kα peak ($\Delta E/E_0 = 0.09$). For the AD-CSCT reconstruction along the vertical scattering direction under $z_d = 120$ mm, the spatial resolution perpendicular and parallel to the beam direction are both determined by the beam spot size $\Delta t = \Delta s = 2$ mm. Considering a scattering angle of 10°, which is roughly the peak position of water in our setup, located at lateral position $t = 0$, the uncertainty in the momentum transfer domain is about $\Delta q_y = 0.01$ Å^{-1}. Notice that for pixels closer to the detector, the momentum transfer uncertainty will become larger and vice versa. We sample the momentum transfer along the y direction at the Nyquist interval 0.005 Å^{-1} in the AD-CSCT reconstruction. Note that the beam hardening of the incident and scattered radiation will further blur the reconstructed scattering profile.

Except for the rotation-invariant radial direction $\psi = 90°$ on the detector, all other radial directions cannot be directly mapped back to the q_r under the corresponding azimuthal angle using conventional AD-CSCT reconstruction, since different 2D momentum transfer sections are probed as projection angle changes. Instead, recovering the scattering profile for all voxels along the beam $f(t, q_r, \psi)$ relies on the inversion of the pencil-beam model described by Eq. (4). However, due to the small scattering angle and limited range of detector movement, direct inverse of the pencil-beam system model in Eq.(4) would result in voxels heavily blurred along the beam, a phenomenon that also appears in Ref. [21]. To decouple the scattering direction from different positions along the beam, prior information on the spatial distribution of the sample obtained from AD-CSCT was used to assist the reconstruction. First, the support of the object was acquired by thresholding the AD-CSCT reconstruction in Fig. 4 (The background is less than 10% of the maximum intensity). We

could then obtain a list of nonzero pixels along each pencil beam by rotating the support to different projection angles. For each pencil beam, all the scattering data under a specific azimuthal angle ψ was extracted from the measurement and stored as $g(w, z_d)_\psi$. Then, based on the discretized forward model matrix $\mathbf{H}$ from Eq. (4), $f(t, q_r)_\psi$ at every azimuthal angle was reconstructed with the object support enforced along dimension t by solving the optimization problem:[23]

$$\widehat{\mathbf{f}} = \arg\min_{\mathbf{f}'} \left(-\log P(\mathbf{g}|\mathbf{f}') + \tau \sum_{i \notin \text{support}} \mathbf{f}'_i\right), \tag{9}$$

where $P(\mathbf{g}|\mathbf{f}')$ is the Poisson likelihood of observing the measurement $\mathbf{g}$ given the parameters $\mathbf{f}'$; τ is the weight for balancing the measurement error and the regularizer, which penalizes the results with large values outside the support. The reconstructions under 2π azimuthal angle ψ were grouped together to form one section of the 3D momentum transfer space $f(t, q_r, \psi)$ along each pencil beam. The five dimensions in sample coordinates were recovered by combining all the pencil-beam positions s and rotation angle ϕ.

Figure 5(a) displays the spatial profile under $q_x = 0.08$ Å^{-1}, which is reconstructed from the $\psi = 0°$ direction on all the scattering images under rotation $\phi = 0°$. Teflon wrap exhibits strong scattering mainly in the y direction due to the formation of molecular chains aligned predominantly along the horizontal direction, where the polymer film is stretched. As a result, Teflon is visible in the spatial profile reconstructed from y direction in Fig. 4(b), but is hardly visible in the spatial profile in Fig. 5(a). The three-dimensional scattering profiles of the pixel marked in green, blue, and red, corresponding to the material of butter, Teflon, and water, are shown in Fig. 5(b1)–5(b3), respectively. The display window of the scattering profile covers $|\mathbf{q}|$ from 0 to 0.3 Å^{-1}. Since butter and water are both noncrystalline material, their scattering intensities depend only on the magnitude of the momentum transfer vector $|\mathbf{q}|$, which agrees with the ring-shaped scattering profile reconstructed from our experiment. Seven sections of the three-dimensional $\mathbf{q}$-space of Teflon wrap ranging from 0° to 180° projection at an angular step of 30° are shown in Fig. 5(c). By enclosing all pixels inside the contour of 70% maximum scattering intensity with minimal bounding circles,[24] the center of two scattering peaks can be extracted, and then, the tilt angle of these two peaks with respect to y axis can, thus, be calculated. The tilt angles of the two strongest scattering spots in the scattering profile against vertical direction are found to be 4.4°, 3.4°, 3.0°, 1.0°, −2.0°, −3.1°, and −4.4°, respectively. The decreasing trend is consistent with the orientation of Teflon wrap projected onto the x-y plane under these rotation angles.

4. DISCUSSION

4.A. Spatial and momentum transfer resolution along non-rotation-invariant directions

It is worthwhile to notice that compared with CSCT, sample rotation plays a different role in our system. In conventional CSCT, rotation assists in resolving the spatial distribution of the sample since the scattering profile of a specific sample voxel is assumed to be consistent along different projection angles. For materials with anisotropic scattering profile, this condition holds only for the scattering intensity along a rotation-invariant direction parallel to the rotation axis, and therefore, only the tomography reconstruction from the $\psi = 90°$ direction on the detector yields the correct spatial profile. For the remaining majority of momentum transfer vectors, separating the scattering profile corresponding to different pixels primarily depends on the inversion of pencil-beam system model, while the function of rotation is limited to probing different sections in the three-dimensional momentum transfer volume.

Here, we would like to further discuss the achievable spatial and momentum transfer resolution from the pencil-beam system model with detector scan along the beam

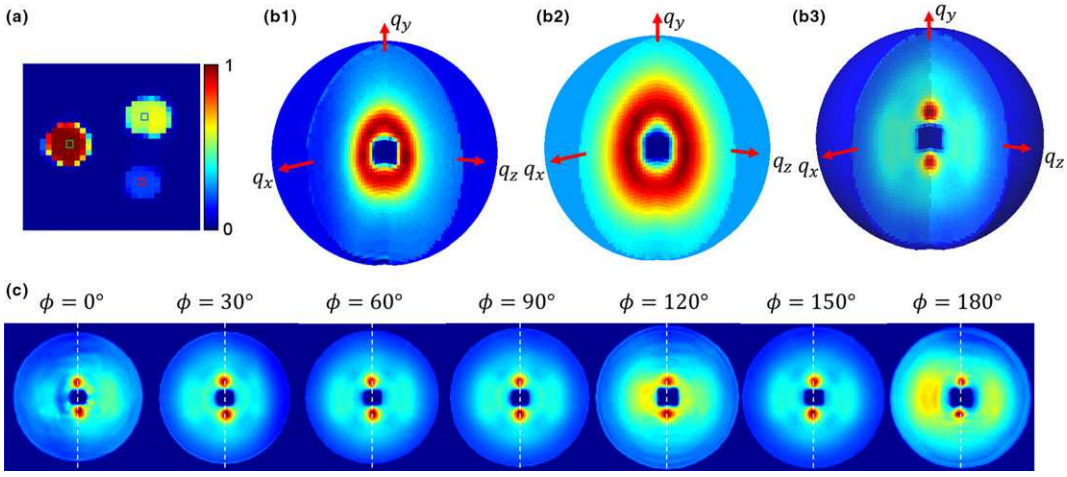

FIG. 5. (a) The spatial profile of the sample under $q_x = 0.08$ Å^{-1}. (b1–b3) Two orthogonal sections in the three-dimensional scattering volume of the pixel in the region of butter, water, and Teflon wrap, respectively. (c) The scattering volume of Teflon is expanded into seven slices under projection angles of 0° to 180° at 30° step. The white, dashed line indicates the y direction to facilitate the display of the orientation of scattering peak as the sample undergoes rotation. The display window of the momentum transfer space is 0–0.3 Å^{-1}. [Color figure can be viewed at wileyonlinelibrary.com]

direction. If we pick a specific radial direction on the detector, each detector pixel located at w from the center of detector captures an integral in the $q_r - t$ domain along a curve defined by Eq. (4). At specific detector position, z_d, all detector pixels along the radial direction constitute a family of curves on the $q_r - t$ plane, with the gradient of the curves determined by z_d. Figure 6(a) demonstrates a series of curves separated by Δw under the smallest and largest z_d, shown in red and blue, respectively. The gradient of these curves increases as the detector is moved closer to the sample. For a specific z_d, the radial intensity distribution $g(w)$ is equivalent to a projection of the 2D object function $f(t, q_r)$ under an angle determined by the gradient. The allowable range of detector movement along z direction confines the gradient of these curves, thus restricting the projection angles in the $q_r - t$ domain, which is analogous to the limited-angle CT problem.[25,26] The location of the voxel and its scattering angle are highly coupled in the $q_r - t$ domain,[27] which cannot be fully decoupled with limited projection angle. The green intersection area in Fig. 6(a) illustrates the achievable resolution Δt~28 mm and Δq_r~0.015 Å^{-1} without any prior information. Figure 6(b1) shows a reconstruction along a single beam penetrating through the Teflon and water under $\phi = 0°$, $\psi = 90°$ by directly inversing the pencil-beam system mode in Eq. (4). Due to the ambiguity in the $q_r - t$ plane, two materials cannot be distinguished along the beam. If the spatial distribution of these two materials are reconstructed from the AD-CSCT measurement and then enforced as the spatial support in the reconstruction of other momentum transfer vectors, the reconstruction, shown in Fig. 6(b2), can distinguish these two materials with the same resolution in reciprocal space as the AD-CSCT. Notice that the spatial and momentum transfer resolution of the pencil-beam system can be further improved using larger detector, thus allowing the detector to move over a wider z_d range without missing the high momentum transfer information.

4.B. Attenuation and beam hardening

In our experiment, we did not correct for the attenuation on the scattered beam due to the relatively small size and simple geometry of the sample. For large objects, the attenuation needs to be calibrated and included in the reconstruction. Eq. (1) contains two mechanisms of attenuation: the reduction of incident photon flux by the voxels upstream the pencil-beam $\alpha(t)$ and the attenuation of scattered photons along the scattering direction $\beta(t, \theta)$. If the scattering angle is small, the scattered beam follows almost the same path as the transmitted beam. Therefore, the self-attenuation can be corrected by normalizing the scattered pattern with transmitted photon flux.[28] When the scattering angle is large, especially under low energies, three-dimensional attenuation map is needed to compensate for the attenuation of the scatted beam.[8]

The attenuation on the low-energy photons by the sample can also cause beam hardening, which shifts the spectrum of the scattered beam to a higher energy than incident spectrum. Our reconstruction was performed under Kα line of copper anode E_0 =8 keV. With the presence of beam-hardening effect, the reconstructed object function in Eq. (1) is distorted by the spectrum $f'(q) = \int S(E) f(q \cdot E/E_0) \mathrm{d}E$, where $f(q)$is directly proportional to the square of molecular form factor. This distortion could cause the shift of the scattering peak to lower momentum transfer, and the loss of fine features in the reconstructed scattering profile. To quantify the beam-hardening effect, 2D energy-sensitive detector array is needed to directly measure the spectrum of scattered photons. The beam hardening can be reduced by switching to a high-energy source with proper filtration, such as molybdenum or silver-anode x-ray tubes.

5. CONCLUSIONS

In summary, we have developed a method to probe the direction-dependent x-ray scattering information inside an extended object. By introducing detector scan along the beam and tomographic data acquisition technique into a

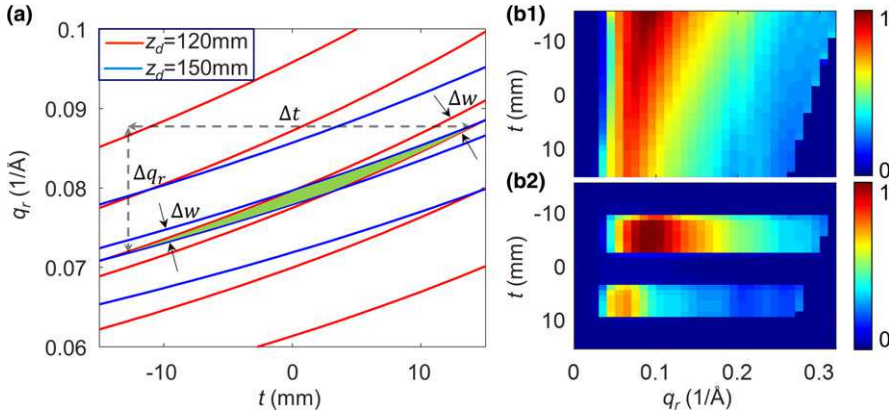

FIG. 6. (a) The intensity on each detector pixel is a line integral on the $q_r - t$ plane. The red and blue families of the lines indicate the detector pixels under different w at z_d = 120 mm and z_d = 150 mm, respectively. (b) Reconstruction from scattering images under different z_d using the pencil-beam system model along a single beam s = 7 mm, rotation angle $\phi = 0$ and $\psi = 90\%$ on the detector: (b1) without enforcing object support (b2) with object support obtained from the CSCT reconstruction. [Color figure can be viewed at wileyonlinelibrary.com]

pencil-beam coherent scattering model, we are able to reconstruct the three-dimensional momentum transfer space of a two-dimensional sample slice. Compared with existing SAXS tomography that preserves anisotropic scattering profile, our proposed setup uses only a table-top x-ray tube and eliminates the tilt of rotation axis, making it easily accessible for biomedical applications. In addition, our method decouples the spatial and momentum transfer space for the non-rotation-invariant directions on the detector. As a result, the number of projections, under which a detector scan along z direction is performed, can be picked based on the number of sections required in 3D q-space. However, given the size of our detector, there is a ~15° missing cone in the 3D q-space that is not covered by our measurement without tilting the sample out of the rotation plane. This imaging modality may find potential biomedical applications including monitoring the tissue regeneration in porous media[13,29] and assessing the bone health via its different compositions.[30] Partially textured SAXS profile could also be used as a contrast mechanism in security screening applications.[31,32] The 3D reciprocal-space coherent scattering tomography could serve as a stand-alone, high-contrast imaging modality in medical imaging, or a secondary screening method in addition to conventional CSCT in case anisotropic scattering signal is present.

ACKNOWLEDGMENTS

The research is supported by the National Science Foundation (DMS-1615124) and Oak Ridge Associated Universities Ralph Powe Junior Faculty Award. The authors have no conflicts to disclose.

[a]Author to whom correspondence should be addressed. Electronic mail: pang@creol.ucf.edu

REFERENCES

1. Ryan EA, Farquharson MJ. Breast tissue classification using x-ray scattering measurements and multivariate data analysis. *Phys Med Biol*. 2007;52:6679.
2. Changizi V, Oghabian MA, Speller R, Sarkar S, Kheradmand AA. Application of small angle x-ray scattering (SAXS) for differentiation between normal and cancerous breast tissue. *Int J Med Sci*. 2005;2:118–121.
3. Fernández M, Keyriläinen J, Serimaa R, et al. Small-angle x-ray scattering studies of human breast tissue samples. *Phys Med Biol*. 2002;47:577–592.
4. Jensen TH, Bech M, Bunk O, et al. Brain tumor imaging using small-angle x-ray scattering tomography. *Phys Med Biol*. 2011;56:1717–1726.
5. Harding G, Kosanetzky J, Neitzel U. X-Ray-Diffraction Computed-Tomography. *Med Phys*. 1987;14:515–525.
6. Westmore MS, Fenster A, Cunningham IA. Tomographic imaging of the angular-dependent coherent-scatter cross section. *Med Phys*. 1997;24:3–10.
7. Schlomka J-P, Harding A, van Stevendaal U, Grass M, Harding GL. Coherent scatter computed tomography: a novel medical imaging technique. In *Medical Imaging 2003*. International Society for Optics and Photonics; 2003:256–265.
8. Kleuker U, Suortti P, Weyrich W, Spanne P. Feasibility study of x-ray diffraction computed tomography for medical imaging. *Phys Med Biol*. 1998;43:2911.
9. Harding A, Schlomka J-P, Harding GL. Simulations and experimental feasibility study of fan-beam coherent-scatter CT. In: *Proc. SPIE 4786*, Penetrating Radiation Systems and Applications IV. Vol 4786.; 2002:202–209.
10. Fratzl P, Jakob HF, Rinnerthaler S, Roschger P, Klaushofer K. Position-resolved small-angle x-ray scattering of complex biological materials. *J Appl Crystallogr*. 1997;2:765–769.
11. Egan CK, Jacques SDMM, Di Michiel M, et al. Non-invasive imaging of the crystalline structure within a human tooth. *Acta Biomater*. 2013;9:8337–8345.
12. Agrawal CM, Ray RB. Biodegradable polymeric scaffolds for musculoskeletal tissue engineering. *J Biomed Mater Res*. 2001;55:141–150.
13. Guldberg RE, Duvall CL, Peister A, et al. 3D imaging of tissue integration with porous biomaterials. *Biomaterials*. 2008;29:3757–3761.
14. Ghammraoui B, Rebuffel V, Tabary J, Paulus C, Verger L, Duvauchelle P. Effect of grain size on stability of X-ray diffraction patterns used for threat detection. *Nucl Instruments Methods Phys Res Sect A Accel Spectrometers, Detect Assoc Equip*. 2012;683:1–7.
15. Cui CW, Jorgensen SM, Eaker DR, Ritman EL. Direct three-dimensional coherently scattered x-ray microtomography. *Med Phys*. 2010;37:6317–6322.
16. Castoldi A, Ozkan C, Guazzoni C, Bjeoumikhov A, Hartmann R. Experimental qualification of a novel x-ray diffraction imaging setup based on polycapillary x-ray optics. *IEEE Trans Nucl Sci*. 2010;57:2564–2570.
17. Cui C, Jorgensen SM, Eaker DR, Ritman EL. Coherent x-ray scattering for discriminating bio-compatible materials in tissue scaffolds. In: Vol 7078.; 2008:70781S–70781S-10.
18. Feldkamp JM, Kuhlmann M, Roth SV, et al. Recent developments in tomographic small-angle X-ray scattering. *Phys Status Solidi A-Applications Mater Sci*. 2009;206:1723–1726.
19. Schroer CG, Kuhlmann M, Roth SV, et al. Mapping the local nanostructure inside a specimen by tomographic small-angle x-ray scattering. *Appl Phys Lett*. 2006;88:164102.
20. Schaff F, Bech M, Zaslansky P, et al. Six-dimensional real and reciprocal space small-angle X-ray scattering tomography. *Nature*. 2015;527:353–356.
21. Terabe M, Okamoto H, Koshida K. Iterative estimation of coherent-scattering profiles from given positions by use of a single-direction beam. *Radiol Phys Technol*. 2012;5:237–247.
22. Pang S, Zhu Z, Wang G, Cong W. Small-angle scatter tomography with a photon-counting detector array. *Phys Med Biol*. 2016;61:3734.
23. Richardson WHWH. Bayesian-based iterative method of image restoration. *J Opt Soc Am*. 1972;62:55–59.
24. Welzl E. Smallest enclosing disks (balls and ellipsoids). In: *New Results and New Trends in Computer Science*; 1991:359–370.
25. Sechopoulos I. A review of breast tomosynthesis. Part I. The image acquisition process. *Med Phys*. 2013;40:14301.
26. Sheng C, Chaudhari R, Rose SD, Sidky EY, Pan X. Choosing anisotropic voxel dimensions in optimization-based image reconstruction for limited angle CT. In: Vol 10132.; 2017:101322X–101322X-5.
27. Pang S, Hassan M, Greenberg J, Holmgren A, Krishnamurthy K, Brady D. Complementary coded apertures for 4-dimensional x-ray coherent scatter imaging. *Opt Express*. 2014;22:22925–22936.
28. Harding G, Kosanetzky J. Elastic scatter computed tomography. *Phys Med Biol*. 1985;30:183–186.
29. Weber L, Langer M, Tavella S, Ruggiu A, Peyrin F. Quantitative evaluation of regularized phase retrieval algorithms on bone scaffolds seeded with bone cells. *Phys Med Biol*. 2016;61:N215–N231.
30. Batchelar DL, Davidson MTM, Dabrowski W, Cunningham IA. Bone-composition imaging using coherent-scatter computed tomography: assessing bone health beyond bone mineral density. *Med Phys*. 2006;33:904–915.
31. Harding G. X-ray scatter tomography for explosives detection. *Radiat Phys Chem*. 2004;71:869–881.
32. Madden RW, Mahdavieh J, Smith RC, Subramanian R. An explosives detection system for airline security using coherent x-ray scattering technology. In: *Proc. SPIE 7079, Hard X-Ray, Gamma-Ray, and Neutron Detector Physics X, 707915*. Vol 7079.; 2008:707911–707915.

ClearCheck

One-click plan evaluation

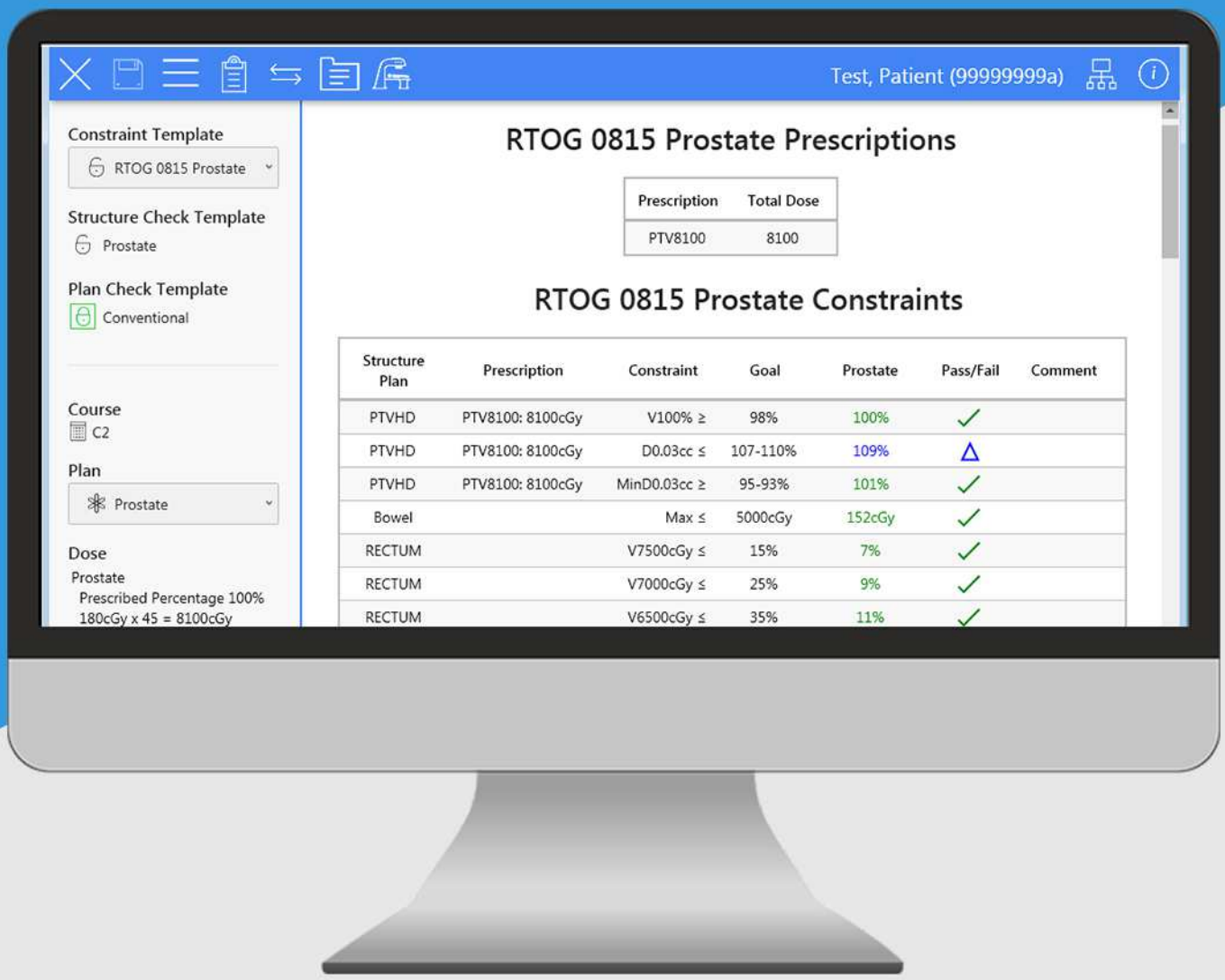

Dose Constraints ◦ Plan Checks

Structure Checks ◦ Collision Checks

RADformation.com